The International Journal of Advanced Manufacturing Technology (2018) 97:641–656
https://doi.org/10.1007/s00170-018-1967-0

ORIGINAL ARTICLE

Trochoidal milling: investigation of a new approach on uncut chip thickness modeling and cutting force simulation in an alternative path planning strategy

Farbod Akhavan Niaki[1] · Abram Pleta[1] · Laine Mears[1]

Received: 6 January 2018 / Accepted: 28 March 2018 / Published online: 8 April 2018

Abstract
Trochoidal milling is an alternative tool path strategy which has been shown to increase productivity, improve tooling life, and reduce resultant cutting forces. While the advantages of trochoidal milling over conventional slot or shoulder milling were previously reported, the complexity of trochoid tool path makes developing an analytical force model highly complicated. In this work, a numerical algorithm to construct the uncut chip thickness model in trochoidal milling is introduced, which is based on the geometrical relation of self-intersection and cross-intersection points of the tool path curve. In addition, an extensive series of experiments is carried out in slot and trochoidal-milling operations in order to investigate the dependency of cutting pressure coefficients on tool path parameters and to develop a model to relate the two. Furthermore, the performance of the developed model for uncut chip thickness and the cutting pressure coefficients are evaluated in predicting cutting forces; it is shown that the model predicts the maximum cutting force in the feed direction and between all the testing sets with 8% total average error, while 17% total average error is observed in predicting maximum cutting force in the lateral direction. This demonstrates the potential of the proposed approach in offline simulation of the cutting forces which is a critical step in selecting proper tooling and process parameters to increase productivity of the cut.

Keywords Trochoidal milling · Slot milling · Uncut chip thickness · Force modeling · Alternative tool path

1 Introduction

Increasing productivity while preserving quality is a key factor in defining the profitability of any manufacturing processes. In past decades, particularly in the metal cutting domain, several approaches have been tested to minimize the loss and increase productivity rate [1]. High-speed machining to increase material removal rate [2], model-based methods of controlling machine parameters to decrease idle time [3, 4], feed rate scheduling to optimize cycle time [5], and process condition monitoring to avoid unscheduled downtime [6] are few examples targeting profitability in machining processes. Recently, with the rapid growth in advanced CAM software that facilitates CNC programming for complex structures, alternative path planning strategies have gained significant momentum within aerospace and energy industries. Trochoidal milling is one such alternative path plan that takes advantage of the superposition of linear and circular revolution of the tool as a material removal strategy.

The need for alternative tool path strategies such as trochoidal milling has been emphasized by the aerospace and energy sectors where extensive use of difficult-to-machine materials such as titanium- or nickel-based alloys is essential. The high strength and poor machinability of these alloys have a significant impact on tooling life and directly influence the quality of the machined part. While the traditional method of reducing machine feed, depth of cut, or replacing the tool in the earlier stages of its life seems intuitive, these approaches adversely affect productivity and increase the machine downtime. Hence, alternative

✉ Farbod Akhavan Niaki
fakhava@clemson.edu

Abram Pleta
apleta@clemson.edu

Laine Mears
mears@clemson.edu

[1] International Center for Automotive Research, Clemson University, Greenville, SC 29607, USA

tool path strategies that increase robustness and extend tool life at more aggressive cutting conditions, such as trochoidal milling, allow for higher depth of cut or feed rates in order to increase the productivity without sacrificing tool life or workpiece quality. Pleta et al. studied the performance of trochoidal milling in comparison to end milling in cutting IN738 nickel-based superalloys [7, 8]. In these studies, the resultant cutting force, tool wear, and surface roughness generated by trochoidal tool paths were compared to end-milling paths. Two metrics were introduced to compare the performance of trochoidal and end-milling cutting strategies: material removal per wear (represents productivity) and material removal rate per wear (represents efficiency). Uhlmann et al. studied the effect of trochoidal milling on energy consumption and material removal rate in cutting Ti-6Al-4V alloy [9]. They concluded that with 6% increase in effective power consumption, 35% reduction in process time can be achieved using trochoidal-milling approach. Rauch et al. studied two aspects of trochoidal milling: implementation on the CNC machine and parameter selection to improve tool life [10]. In [11], the performance of trochoidal milling in terms of cutting force and tool wear was investigated in milling mold cavities. In another effort by Szaloki et al., resultant force, surface roughness, and micro-geometrical error were studied, and empirical relations were developed for each parameter [12]. A modified tool path termed the *epicycloid path* inspired from the trochoidal path was introduced in [13], and machining force, vibration, and cycle time were experimentally compared to trochoidal-milling tool path. The authors in [13] concluded that epicycloidal milling can increase the cycle time by 20% while higher force and vibration adversely affect tool life.

Many articles published on this topic are mainly focused on the advantages of trochoidal milling over traditional milling strategies (e.g., slot or pocket) in terms of cycle time, resultant force, and tooling life. While establishing the benefits of alternative tool path plans is essential to justify the potentials of trochoidal milling to replace the traditional methods, a comprehensive study is not yet available on the mechanics and dynamics of trochoidal milling. To the best of the authors' knowledge, there are currently only two articles addressing the mechanics of trochoidal milling. Otkur and Lazoglu published the first article on chip thickness modeling and force simulation in trochoidal milling [14]. In their work, they introduced a closed form uncut chip thickness formulation based on the geometry of the cut and further simulated the cutting force in X and Y directions in trochoidal and double trochoidal milling (where the circular downward revolution of the tool is followed by an upward revolution). In the second article published by Kardes and Altintas, the trochoidal tool path was introduced with an alternative name, circular milling [15], and the same approach of [14] was taken to model the uncut chip thickness. In addition, the dynamic stability of the trochoidal milling was investigated with frequency domain and time finite element analysis and the differences of the two approaches in predicting the critical depth of cut to avoid chatter were highlighted.

Two major shortcomings exist in the methods described in [14, 15]. First, in both articles, it was assumed the outer margin generated by the trochoidal tool path can be approximated by a circular curve; it will be discussed later in this article that the departure from this circular assumption can introduce significant error. Second, to simulate the cutting forces, both articles relied upon on the pre-existing values for tangential and radial cutting pressure coefficients extracted from slot-milling experiments. However, there are essential differences in the mechanics of cutting and chip generation between slot and trochoidal milling which will be highlighted in detail in this work. Based on these shortcomings, the objective of this paper is defined as (1) introducing a new geometrical and generalized approach based on constructing the chip area through intersection points of the trochoid tool path without the assumption of circular outer margin; (2) investigating the effect of trochoidal tool path and process parameters on cutting pressure coefficients and highlighting the differences with traditional milling strategy (i.e., slot milling); and (3) evaluating the performance of the proposed modeling framework in predicting cutting forces during trochoidal milling. The organization of this work is as follows: the geometrical approach will be introduced in Section 2 for single-tooth and multi-tooth tools. In Section 3, the mechanistic force model is given. The experimental setup and design of experiment are discussed in Section 4. The identification of cutting pressure coefficients in trochoidal and slot-milling tests and dependency on tool path parameters are given in Section 5. In Section 6, the simulated force under different cutting conditions is compared with experimentally measured forces, and corresponding error is quantified; this is followed by conclusions and future direction discussion in Section 7.

2 Geometric approach for uncut chip thickness modeling in trochoidal tool path

2.1 Mathematical representation of trochoidal tool path

The trochoidal tool path can be characterized with three parameters: (1) *rotational rate* ($\dot{\theta}$), which represents the rotational speed of the tool holder in RPM and clockwise direction; (2) *nutational rate* ($\dot{\phi}$), which represents the revolutionary (or planetary) motion of the tool center in

rad/s and counterclockwise direction; and (3) *step-over feed rate* (ν) in unit of mm/s and in Y direction which represents the linear motion of the tool center. The combination of these three parameters shown in Eqs. (1) and (2) produces a trochoidal tool path, where, R_{cp} is radius of the tool center in mm, R_t is cutting tool radius in mm, t is time in second, and $[X_t\ Y_t]^T$ is the global coordinate of the cutter tip in the X–Y plane. Note that in mathematical society, the curve generated from Eqs. (1) and (2) is known as *epitrochoidal curve* [16]; however, in manufacturing society, it is widely known as trochoidal curve (a term used in the rest of this paper).

The geometrical representation of trochoidal tool path is given in Fig. 1a. Unlike the general belief that the trochoidal tool path generates an approximately circular outer margin (termed *outer lobe*, in the rest of this article), the existence of step-over feed rate (ν) in Eq. (2) generates a skewed outer lobe. As shown in Fig. 1b, with advancement of the tool in the + Y direction, a larger deviation is produced between the trochoidal outer lobe and circular path assumption. By increasing $\dot{\theta}$ and decreasing $\dot{\phi}$, continuity and smoothness of the outer lobe will be improved. However, the assumption of a purely circular outer lobe still remains invalid except in the case of very small step-over feed rates.

$$X_t = R_{cp}\cos(\dot{\phi}t) + R_t\cos\left(-\frac{2\pi}{60}\dot{\theta}t\right) \tag{1}$$

$$Y_t = R_{cp}\sin(\dot{\phi}t) + R_t\sin\left(-\frac{2\pi}{60}\dot{\theta}t\right) + \nu t \tag{2}$$

Unlike traditional milling (e.g., shoulder or slot milling), where the geometry of each chip remains consistent throughout the cut, in trochoidal milling, each chip's geometry is different from every other due to combination of nutation (planetary motion) and step-over feed rates (linear motion). In addition, due to the mathematical complexity of Eqs. (1) and (2), a closed form solution for describing chip geometry is not available. However, as shown in Fig. 2, where the tool path for two consecutive nutations is shown, it is possible to represent chip geometry if the coordinates of the intersection points of the tool path curve are known. In Fig. 2, the first nutation path is named *previous path* and the second nutation is named *current path* (which represents the current coordinate of the cutter). Knowing the self-intersecting and cross-

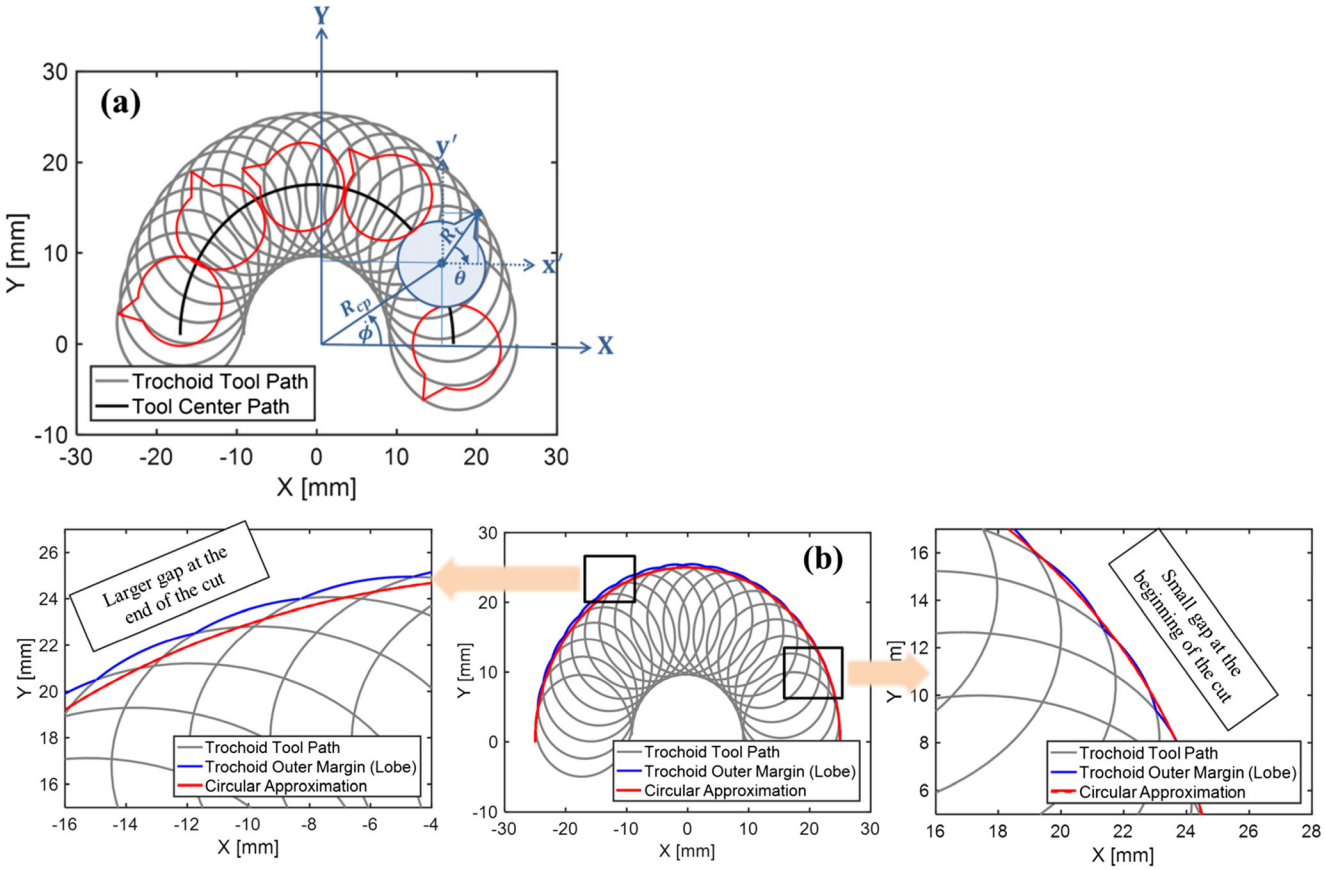

Fig. 1 Trochoidal tool path for single-flute cutter; **a** geometrical representation with tool rotation rate ($\dot{\theta}$) and nutation rate ($\dot{\phi}$), and **b** deviation between trochoidal and circular tool paths

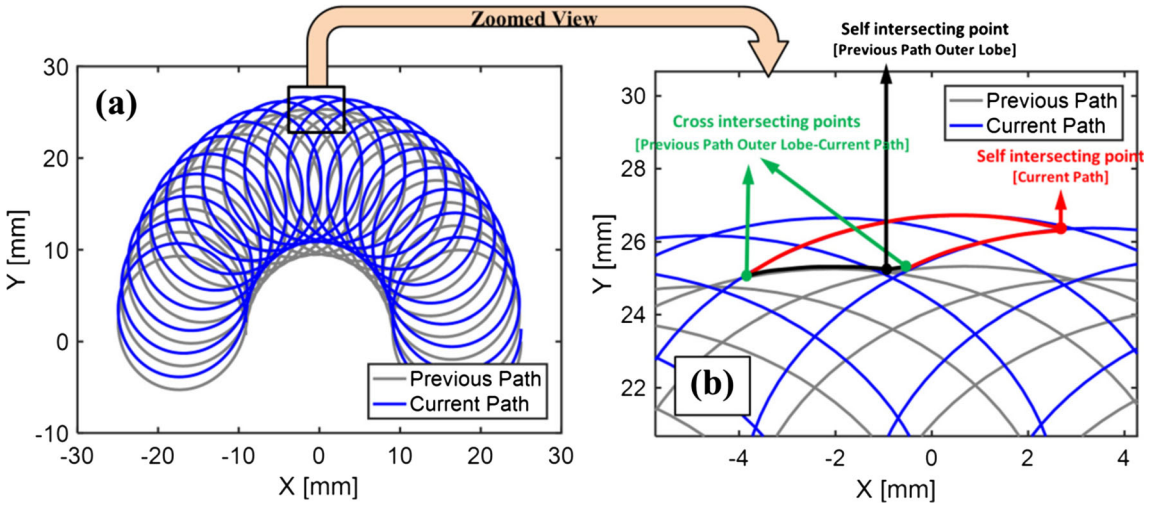

Fig. 2 Trochoid tool path in single-tooth cutter with $\dot{\theta} = 600$ RPM, $\dot{\phi} = \pi/2$ rad/s, and $\nu = 0.35$ mm/; **a** geometry of each chip varies with the nutational motion of the tool center and **b** proper connection of cross- and self-intersection points defines chip geometry

intersecting points of the current and previous paths given in Fig. 2b, the chip geometry can be constructed.

2.2 Numerical algorithm for identification of intersection points

In order to find the intersection points (self- or cross-intersection), the trochoid curve is discretized into several linear curves with the length dL in time (dt) which is demonstrated with an exaggerated offset in Fig. 3a. From the mathematical standpoint, if two lines are not parallel, they must have an intersection point. However, in the context of this paper, an intersection point between any two arbitrary line segments is "desirable" when its coordinates satisfying the inequality conditions of Eq. (3), where $[x_p\ y_p]^T$ is the coordinate of the intersection point, i is an integer representing either the first or second line segment, $[x_{is}\ y_{is}]^T$ is the starting point, and $[x_{if}\ y_{if}]^T$ is the end point of each line segment. In a matrix format, the point $[x_p\ y_p]^T$ in Fig. 3b is a "desired" intersection point between any pair of line segments if and only if the matrix inequality shown on the right side of Eq. (3) becomes less than unity.

$$\begin{pmatrix} x_{1s} < x_p < x_{1f} \\ x_{2s} < x_p < x_{2f} \\ y_{1s} < y_p < y_{1f} \\ y_{2s} < y_p < y_{2f} \end{pmatrix} \Leftrightarrow \begin{bmatrix} \dfrac{\mathrm{d}LT_1}{\mathrm{d}L_1} \\ \dfrac{\mathrm{d}LT_2}{\mathrm{d}L_2} \end{bmatrix} \leq 1 \tag{3}$$

Considering the geometrical relation between any pair of line segments shown in Fig. 3b, two independent equations in X and Y directions for each line can be written and converted into matrix format as in Eq. (4). The unknowns of this linear equation are the coordinates of intersection point and length ratios (dLT_i/dL_i). After finding the solution of Eq. (4) and if the $[x_p\ y_p]^T$ point satisfies the condition in Eq. (3), it will be selected as a "desirable" intersection point. To avoid the curse of

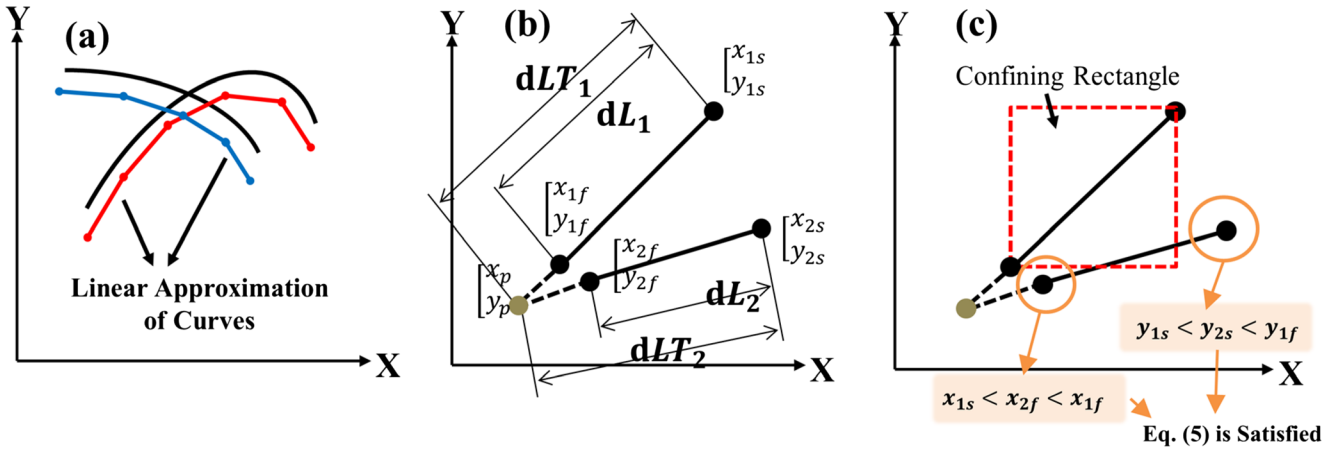

Fig. 3 Numerical method of finding intersection points; **a** exaggerated discretization of curves into linear segments, **b** an "un-desired" intersection point between a pair of arbitrary line segment, and **c** confining rectangular zone to reduce computational cost

dimensionality and improve the performance of this brute force algorithm, only the lines that satisfy the condition in Eq. (5) will be selected. This inequality is equivalent to drawing a confining rectangular zone around a selected line segment and check to see if the start and end points of the other line belong to this zone or not (see Fig. 3c).

$$\begin{aligned}
&\frac{dLT_1}{dL_1}\left(x_{1s}-x_{1f}\right)=\left(x_{1s}-x_p\right)\\
&\frac{dLT_1}{dL_1}\left(y_{1s}-y_{1f}\right)=\left(y_{1s}-y_p\right)\\
&\frac{dLT_2}{dL_2}\left(x_{2s}-x_{2f}\right)=\left(x_{2s}-x_p\right)\\
&\frac{dLT_2}{dL_2}\left(y_{2s}-y_{2f}\right)=\left(y_{2s}-y_p\right)
\end{aligned}
\rightarrow
\begin{bmatrix}
\frac{dLT_1}{dL_1}\\
\frac{dLT_2}{dL_2}\\
x_p\\
y_p
\end{bmatrix}$$

$$=\begin{bmatrix}
x_{1s}-x_{1f} & 0 & 1 & 0\\
y_{1s}-y_{1f} & 0 & 0 & 1\\
0 & x_{2s}-x_{2f} & 1 & 0\\
0 & y_{2s}-y_{2f} & 0 & 1
\end{bmatrix}^{-1}
\begin{bmatrix}
x_{1s}\\ y_{1f}\\ x_{2s}\\ y_{2f}
\end{bmatrix} \tag{4}$$

$$\begin{cases}
x_{1s} < x_{2s} < x_{1f}\\
\text{or}\\
x_{1s} < x_{2f} < x_{1f}
\end{cases}
\text{and}
\begin{cases}
y_{1s} < y_{2s} < y_{1f}\\
\text{or}\\
y_{1s} < y_{2f} < y_{1f}
\end{cases} \tag{5}$$

2.3 Chip geometry construction from intersection points

Assuming a single-point cutter, the first step after finding all the intersection points is to construct the outer lobe region generated from self-intersecting points of the previous tool path. Equation (6) is used to generate a *push curve* encompassing the outer lobe of the previous pass, where $[X_c\ Y_c]^T$ is the coordinate of the push curve. The self-intersecting points with the minimum distance to the push curve are selected and properly connected to construct the outer lobe which is shown in Fig. 4. Note that, due to existence of the term vt in Eq. (6), the push curve does not represent a circular curve but it is rather a skewed circular curve in feed direction.

$$\begin{aligned}
X_c &= \left(R_{cp} + R_t\right)\cos\left(\dot{\phi}t\right)\\
Y_c &= \left(R_{cp} + R_t\right)R_{cp}\sin\left(\dot{\phi}t\right) + vt
\end{aligned} \tag{6}$$

The second step is to use the intersection algorithm to find the cross-intersection points between the current path and the outer lobe. Here, the cross-intersection points are critically important since the chip geometry begins with these points (see the selected points in Fig. 2b). The third step is similar to the first step, but instead, it will be conducted to find the self-intersecting points of the current path. At this stage, all the corner points of a chip are identified, and the geometry can be constructed by proper connection of these points.

Considering from Fig. 5a, any chip geometry (e.g., chip number $\{N\}$) can be defined by three regions:

(1) Region 1 ($R_1^{\{N\}}$), which is defined based on marching from point $A_1^{\{N\}}$ (cross-intersection point between the outer lobe and the current path) to the point $A_{22}^{\{N\}}$ (second self-intersection point on the outer lobe of current path).
(2) Region 2 ($R_2^{\{N\}}$), which is a partial region of $R_1^{\{N-1\}}$, generated by the previous chip $\{N\text{-}1\}$, and is defined based on marching from point $A_1^{\{N-1\}}$ to the point $A_2^{\{N-1\}}$.
(3) Region 3 ($R_3^{\{N\}}$), which is defined based on marching from point $A_1^{\{N\}}$ to the point $A_1^{\{N-1\}}$ on the outer lobe of the previous path.

Note that the points $A_{22}^{\{N\}}$ and $A_2^{\{N-1\}}$ have in fact the same coordinates. For chip $\{N\}$, $A_{22}^{\{N\}}$ is the second self-intersection point (the first is denoted as $A_2^{\{N\}}$) that defines $R_1^{\{N\}}$, while $A_2^{\{N-1\}}$ is the first self-intersection point of chip $\{N-1\}$ used to define $R_2^{\{N\}}$. Following this algorithm, the exact geometry of each chip can be constructed properly for single-tooth

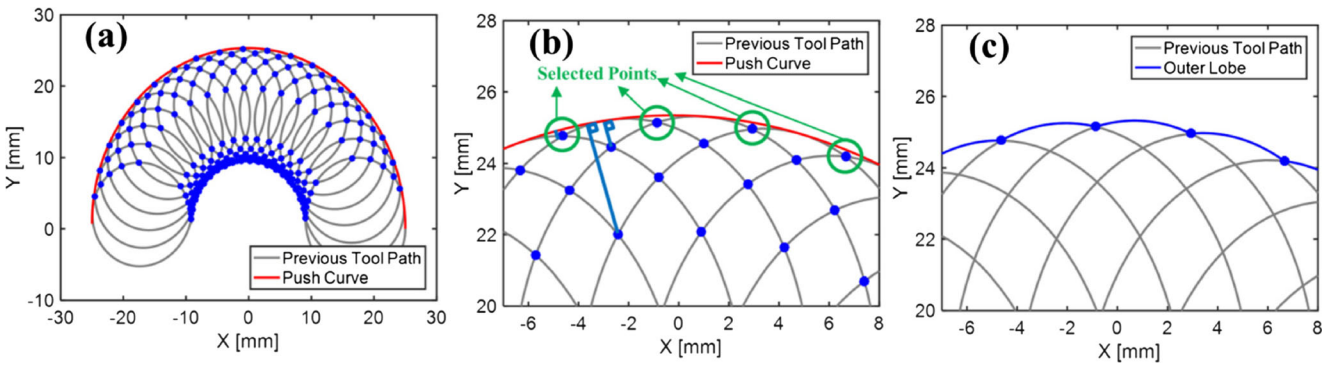

Fig. 4 Constructing the outer lobe from previous tool path, **a** self-intersecting point identification, **b** selecting points closest to the push curve, and **c** connecting points to construct outer lobe

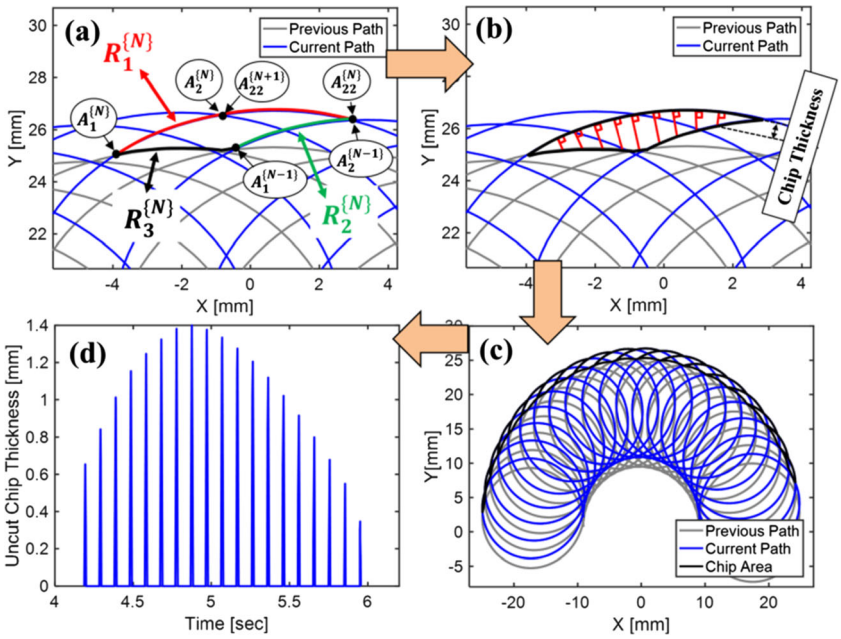

Fig. 5 Chip geometry construction in trochoidal milling; **a** identification of regions of interest, **b** uncut chip thickness calculation, **c** uncut chip area construction, and **d** uncut chip thickness evolution with respect to time

cutters, and the thickness profile quantified. As demonstrated in Fig. 5b, uncut chip thickness is the perpendicular distance of the points on R_2 and R_3 regions to the R_1 region. The associated time for each chip is defined as the time the cutter enters the chip through point $A_1^{\{N\}}$ (start of the cut) with $\theta_s^{\{N\}}$ entering angle until the time the cutter exists within the chip from point $A_{22}^{\{N\}}$ with $\theta_e^{\{N\}}$ exiting angle. The identified uncut chip area and the corresponding uncut chip thickness evolution in time are depicted in Fig. 5c–d for a single-cutter tool.

2.4 Uncut chip thickness modeling of multi-tooth and variable spacing tools

Without loss of generality, the method described in Section 2.3 can be extended to tools with multi- and/or variable spacing cutters. The main difference of these with the single-tooth scenario is that in the trochoidal path of multi-cutter tools, the outer lobe of the previous path is not constructed through self-intersecting points. Since the motion of the first cutter is followed by the second cutter and so on, to construct the outer lobe, only cross-intersecting points are required to be identified between each of the cutter paths. To better clarify this, the trochoid path equation for a tool with three teeth and equal spacing is given in Eqs. (7) and (8), where parameter δ represents the angular location of the cutter. As depicted in Fig. 6a, the outer lobe is constructed by connection of cross-intersecting points of each cutter path. To produce the chip geometry, the rotational direction of the tool plays an important role. As shown in Fig. 6b, with clockwise rotation of the tool, the R_2 region of the first cutting edge is generated based on the path of third cutting edge, the R_2 region of the second cutting edge is generated based on the path of the first cutting edge, and the R_2 region of the

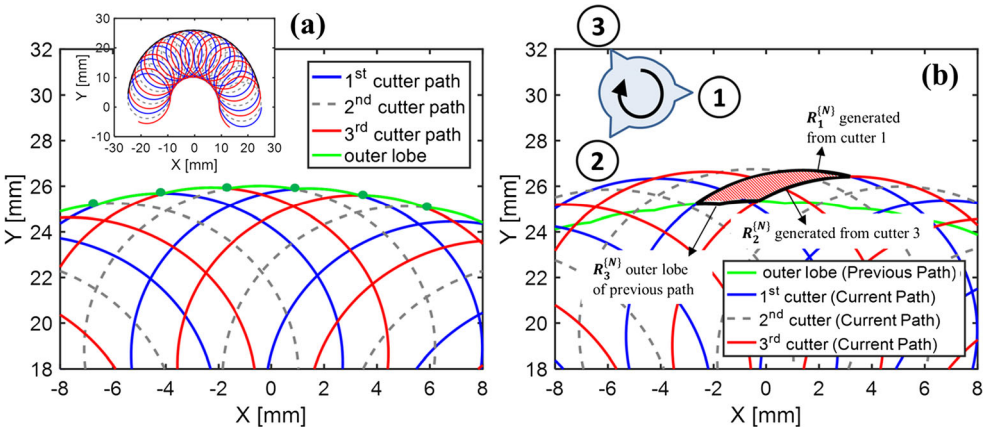

Fig. 6 Trochoidal tooth path in three-cutter tool with θ = 600 RPM, $\dot{\phi} = \pi/2$ rad/s, and ν = 0.35 mm/s. **a** Outer lobe is the combination of cross-intersecting points of each cutter, and **b** $R_2^{\{N\}}$ of chip geometry for the first cutting edge is generated from the third cutting-edge path

third cutting edge is generated based on the path of the second cutting edge. To construct the chip geometry, the same procedure as described in Section 2.3 should be followed.

$$X_t = R_{cp}\cos(\dot{\phi}t) + R_t\cos\left(-\frac{2\pi}{60}\dot{\theta}t - \delta\right) \quad \text{where} \quad \delta\in\left\{0, \frac{2\pi}{3}, \frac{4\pi}{3}\right\} \tag{7}$$

$$Y_t = R_{cp}\sin(\dot{\phi}t) + R_t\sin\left(-\frac{2\pi}{60}\dot{\theta}t-\delta\right) + vt \quad \text{where} \quad \delta\in\left\{0,\frac{2\pi}{3},\frac{4\pi}{3}\right\} \tag{8}$$

3 Cutting force calculation in trochoidal milling

Using the uncut chip thickness modeling method described in Section 2.2, the uncut chip area at any time can be calculated based on the product of uncut chip thickness, denoted as $h(t)$, and axial depth of cut denoted as b in Eq. (9). Here, the function $g(t)$ is "1" when the cutter is engaged in the cut and "0" in no-cut regions (see Eq. (10)). The semi-mechanistic cutting force model in the tangential and radial directions is taken from [17] and is given in Eq. (11), where K_t and K_r are tangential and radial cutting pressures, and K_{te} and K_{re} are edge coefficients representing the sliding frictional force due to tool wear. Having access to the instantaneous cutter angle $\theta^{\{N\}}$, the cutting forces from local coordinates are converted to cutting forces in X–Y global coordinates with the rotation matrix R in Eq. (12). The local and global coordinates and angle of rotation for an arbitrary chip are shown in Fig. 7. Note that the positive direction of the forces in X–Y coordinates is imposed by the positive direction of the dynamometer.

$$A^{\{N\}}(t) = bh^{\{N\}}(t)g^{\{N\}}(t) \tag{9}$$

$$g^{\{N\}}(t) = \begin{cases} 1 & \text{when} \quad t_s^{\{N\}} < t < t_e^{\{N\}} \\ 0 & \text{when} \quad t < t_s^{\{N\}}, t > t_e^{\{N\}} \end{cases} \tag{10}$$

$$\begin{aligned} F_T &= K_t bh^{\{N\}}(t)g^{\{N\}}(t) + K_{te}b \\ F_R &= K_r bh^{\{N\}}(t)g^{\{N\}}(t) + K_{re}b \end{aligned} \tag{11}$$

$$[F_X \quad F_Y]^T = \begin{bmatrix} -\sin\left(\theta^{\{N\}}\right) & -\cos\left(\theta^{\{N\}}\right) \\ -\cos\left(\theta^{\{N\}}\right) & \sin\left(\theta^{\{N\}}\right) \end{bmatrix} [F_T \quad F_R]^T \tag{12}$$

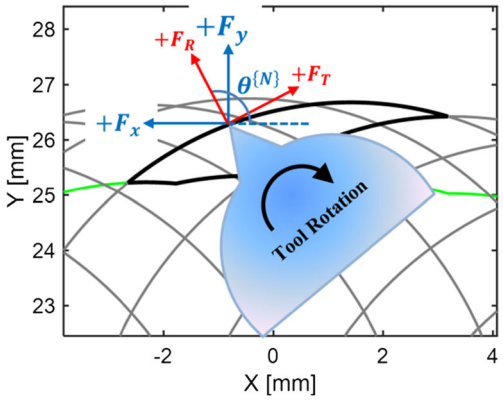

Fig. 7 Positive orientation of the cutting forces in in X–Y coordinates and angle of rotation $\theta^{\{N\}}$

4 Experimental setup

The physical testing was performed on an Okuma MU-5000 V machine using a Kistler 9257B piezoelectric dynamometer with a sampling frequency of 2 kHz. As stated in Section 1, one of the objectives of this work is to investigate the dependency of the cutting pressure coefficients on the tool path. In other words, we are seeking the possibility to use slot or shoulder-milling tests to identify these coefficients and use them in trochoidal milling in order to predict forces. To answer this question, a comprehensive testing strategy was designed to compare slot milling (with full radial engagement) and trochoidal milling. To preserve the stability of the cut, it was decided to use a two-flute indexable end mill for each slot-milling experiment.

The trochoidal-milling tests for identification of cutting pressure coefficients were conducted with a single-flute indexable end mill, while the tests designed for validating the accuracy of the uncut chip thickness model in predicting cutting forces were conducted with the same two-flute tool used in slot-milling tests. All of the experiments were carried out with sharp (unused) Sandvik Coromill R390-11T308M-PM-1030 carbide insert with multilayer TiAlN coating and axial depth of cut of 0.5 mm. The tooling utilized had a lead angle of 90°, an axial rake angle of 12.4°, and a radial rake angle of 2.5°. To ensure the repeatability of the tests, all the experiments were repeated three times.

While the capability of trochoidal milling is best put to use in cutting hard-to-machine materials such titanium- or nickel-based alloys, the excessive wear generation during machining these materials hinders validation of the proposed uncut chip thickness modeling strategy. Hence, it was decided to perform all the testing on 7075-T6 aluminum to eliminate any tool wear effects on the results. Due to the minimal wear, the cutting-edge coefficients, K_{te} and K_{re}, in Eq. (11) are set equal to zero. As shown in Eqs. (1) and (2), the trochoidal tool path is defined with three parameters: θ, $\dot{\phi}$, and ν. The parameter θ is understood by the CNC machine as rotational speed;

Table 1 Design of experiment for trochoidal path with single-flute tool (three replications for each test)

Number (#)	Trochoidal tool path parameters		CNC machine equivalent parameters			
	Step-over feed rate, ν (mm/s)	Nutation rate, $\dot{\phi}$ (rad/s)	Rotational rate, $\dot{\theta}$ (RPM)	Axial depth of cut, b (mm)	Equivalent feed rate, f_r (mm/min)	Feed per tooth, f (mm/tooth)
ITS-1	0.05	0.64	300	0.5	729.6	2.43
ITS-2	0.05	0.64	600	0.5	729.6	1.22
ITS-3	0.05	0.64	900	0.5	652.8	0.36
ITS-4	0.05	0.64	1000	0.5	652.8	0.33
ITS-5	0.05	0.64	1100	0.5	652.8	0.30
ITS-6	0.05	0.64	1200	0.5	729.6	0.61
ITS-7	0.05	0.64	1300	0.5	652.8	0.27
ITS-8	0.05	0.64	1450	0.5	652.8	0.25

however, parameters $\dot{\phi}$ and ν should be converted to machine feed rate (f_r) in mm/min in order to make G-code programming possible. The conversion is carried out by dividing the tool center travel (directly affected by parameters $\dot{\phi}$ and ν—see black curve in Fig. 1) to the time of travel. In this way, machine feed rate (f_r) and feed per tooth (f) can be calculated for the trochoid tool path.

In this work, three separate designs of experiment (DoEs) are conducted. The first DoE shown in Table 1 is created for comparison of cutting pressure coefficients between trochoidal and slot-milling tests. In these tests, the step-over feed rate and nutation rate were kept constant, and rotation rate was varied. For slot-milling tests, an equivalent DoE to trochoidal-milling tests is employed, as given in Table 2. The first series (CFC6) was selected with the same cutting conditions as trochoidal-milling single-flute tests of Table 1 (equal rotation rate, feed per tooth, and axial depth of cut). In the CFC6 test series, despite the fact that the feed per tooth is equivalent to the feed per tooth of trochoidal tests, the maximum and average uncut chip thickness values are different from the trochoidal tests. Therefore, two additional series of slot-milling experiments (named CFC7 and CFC9) are designed to match the maximum and average uncut chip thickness of trochoidal tests to slot-milling tests. The procedure for the determination of feed per tooth for this two series is described below:

(1) For each test number in Table 1, the maximum (h_{max}) and average uncut chip thickness (h_{avg}) were calculated using the numerical algorithm described in Section 2 (see Fig. 5d).
(2) In CFC7 tests, the feed per tooth is equal to the calculated maximum uncut chip thickness (h_{max}) of the trochoidal test.
(3) In CFC9 tests, the feed per tooth is equal to the product of $\pi/2$ and the average uncut chip thickness (h_{avg}) of the trochoidal test.

The third DoE was created in variable nutation and rotation rates to test the performance of the proposed method

Table 2 Design of experiment for slot milling with double-flute tool (three replications for each test)

Number (#)	Rotational rate, $\dot{\theta}$ (RPM)	Axial depth of cut, b (mm)	Feed per tooth, f (mm/tooth)		
			CFC6	CFC7	CFC9
IS-1	300	0.5	2.43	0.41	0.51
IS-2	600	0.5	1.22	0.31	0.43
IS-3	900	0.5	0.81	0.23	0.31
IS-4	1000	0.5	0.73	0.21	0.28
IS-5	1100	0.5	0.66	0.20	0.26
IS-6	1200	0.5	0.61	0.18	0.24
IS-7	1300	0.5	0.56	0.17	0.23
IS-8	1450	0.5	0.50	0.15	0.21

Table 3 Design of experiment for evaluating uncut chip thickness model with single- and two-flute tools (three replications for each training set and one replication of testing set)

Number (#)		Step-over feed rate, ν (mm/s)	Nutation rate, $\dot{\phi}$ (rad/s)	Rotational rate, $\dot{\theta}$ (RPM)	Axial depth of cut, b (mm)
Training set (single-flute)	TS-1	0.05	0.16	300	0.5
	TS-2	0.05	0.32	300	0.5
	TS-3	0.05	0.64	300	0.5
	TS-4	0.05	0.16	600	0.5
	TS-5	0.05	0.32	600	0.5
	TS-6	0.05	0.64	600	0.5
	TS-7	0.05	0.16	1200	0.5
	TS-8	0.05	0.32	1200	0.5
	TS-9	0.05	0.64	1200	0.5
Testing set (two-flute)	TD-1	0.05	0.64	900	0.5
	TD-2	0.05	0.64	1000	0.5
	TD-3	0.05	0.64	1300	0.5
	TD-4	0.05	0.64	1450	0.5

of uncut chip thickness calculation in predicting forces. As shown in Table 3, using the tests in the training set, a linear regression model between the identified cutting force coefficients (K_t and K_r) and trochoidal parameters ($\dot{\phi}$ and $\dot{\theta}$) will be developed. Later, the regression model will be used in the testing set to find cutting pressure coefficients and cutting forces will be simulated using the method described in Sections 2 and 3. Note that all the experiments in the testing set were conducted with a two-flute tool using the rotational rates not used in developing the regression model from the training set.

5 Identification of cutting pressure coefficients

The objective of this section is to investigate if cutting pressure coefficients extracted from the slot milling can be used interchangeably for predicting forces in trochoidal milling. The experiments used here are from Table 1 and Table 2, namely tests ITS-1–8 and tests IS-1–8. The cutting pressure coefficients K_t and K_r can be found by using Eq. (12) to convert measured cutting forces in the X and Y directions into tangential and radial directions and then dividing F_T and F_R by the chip area (again, K_{te} and K_{re} are considered zero as described in Section 4). An example of the measured cutting forces and simulated uncut chip thickness is shown in Fig. 8 for test ITS-1, where cutting pressure coefficients are calculated by considering ten consecutive rotations of the tool. The same process is repeated for slot-milling tests (IS-1–8). However, in this case, the chip area can be analytically described with the function $bf\sin(\alpha(t))$ where α is instantaneous cutter angle. Since all the tests in Table 2 have been carried out in full radial engagement, the parameter α varies from 0° (entering the cut) and 180° (exiting the cut).

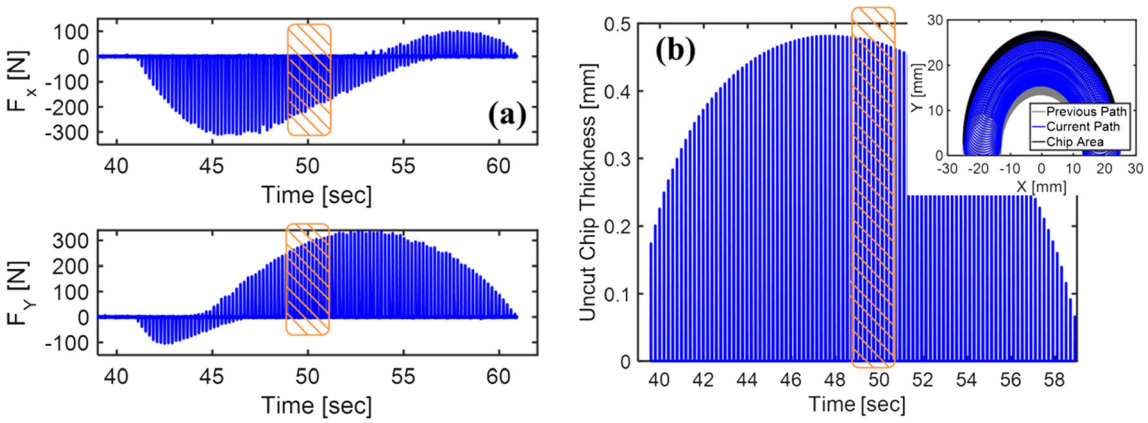

Fig. 8 Cutting pressure identification requires force measurement and chip area calculation—forces and corresponding chips are selected for ten tool rotations [hatched rectangle]; **a** measured cutting force in X–Y directions for test ITS-1, and **b** simulated uncut chip thickness for test ITS-1

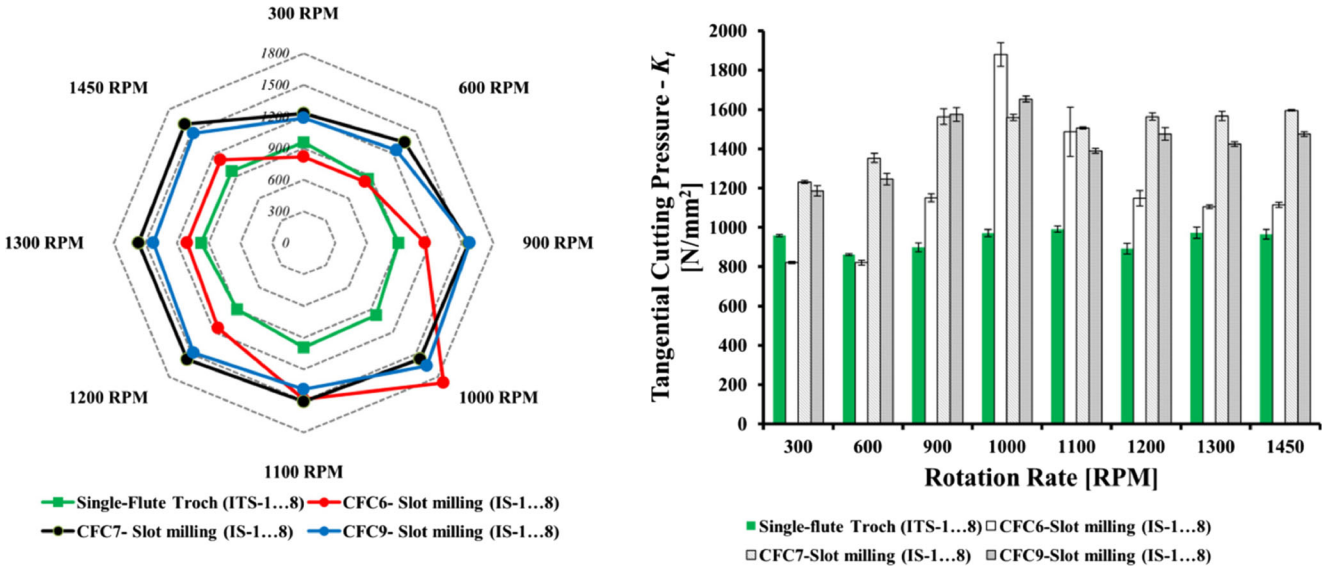

Fig. 9 Identified tangential cutting pressure coefficients (K_t) between trochoidal-milling tests and slot-milling test series

5.1 Comparison of cutting force coefficients in slot and trochoidal milling

The comparison is made in Figs 9 and 10 using radar and bar graphs. As demonstrated in these figures, significant error exists between cutting pressure coefficients derived from trochoidal and slot-milling test series of CFC7 and CFC9. The average error between all the milling tests (IS-1–8) of each series and trochoidal tests (ITS-1–8) is given in Table 4, where 59 and 52% difference errors were observed in K_t and 28 and 27% difference errors were observed in K_r as derived from tests CFC7 and CFC9. However, the CFC6 test shows somewhat better performance in predicting tangential cutting pressure with 31% difference error and somewhat worse performance in predicting radial cutting pressure with 51% difference error. As demonstrated in the radar graphs of Figs. 9 and 10, in general, using slot-milling experiments for finding cutting pressure coefficients leads into an overprediction in tangential cutting pressure (K_t) and an underprediction in radial cutting pressure (K_r). As a result and contrary to what was used in [14, 15], the cutting pressure coefficients derived from slot-milling tests should not be replaced as cutting pressure coefficients of trochoidal milling.

The argument here is that there is still an essential difference in the mechanics of cutting between trochoidal and slot milling. As shown in Fig. 7, trochoidal milling is categorized as a low to medium radial immersion cutting process (this is the reason higher feed rates with less chip load and less chance

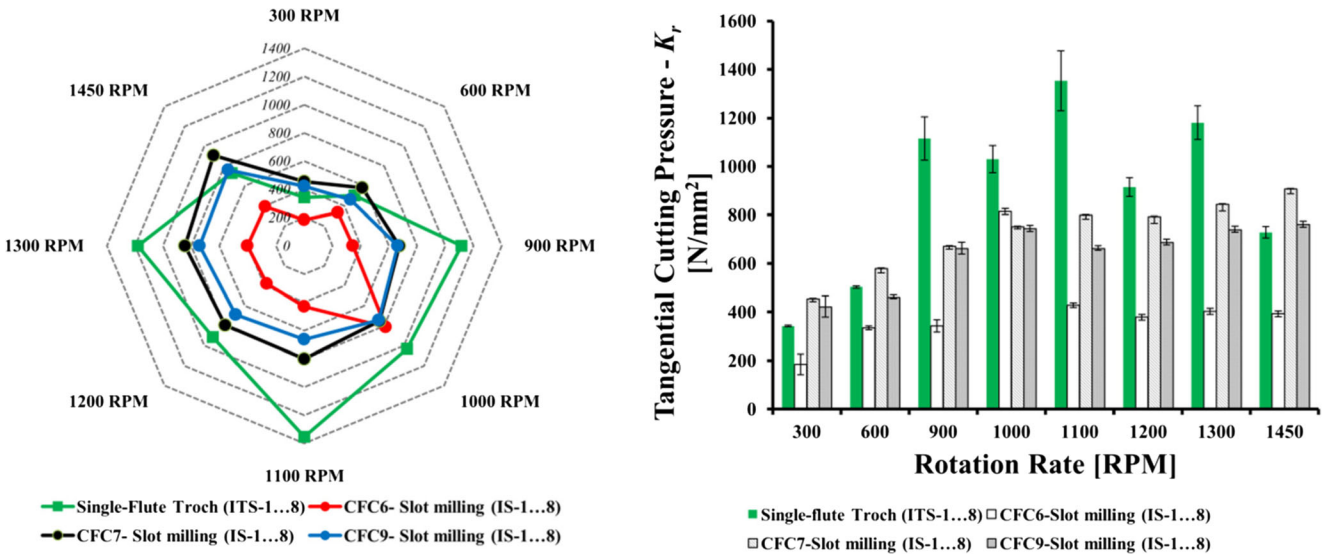

Fig. 10 Identified radial cutting pressure coefficients (K_r) between trochoidal-milling tests and slot-milling test series

Table 4 Comparison of average error between cutting pressure coefficients of slot-milling tests and trochoidal milling (all errors given in percentage)

Error difference with respect to trochoidal milling (%)	K_t (N/mm^2)			K_r (N/mm^2)		
	CFC6	CFC7	CFC9	CFC6	CFC7	CFC9
IS-1	14	28	24	46	33	23
IS-2	5	57	45	33	15	8
IS-3	28	74	75	69	40	41
IS-4	94	61	70	21	27	28
IS-5	50	52	40	68	41	51
IS-6	29	75	66	59	13	25
IS-7	14	61	46	66	28	37
IS-8	16	65	53	46	25	5
Average error (%)	31	59	52	51	28	27

of tool breakage can be achieved in trochoidal milling). However, all the milling tests in this work were conducted in full radial immersion. As reported in [18], with lower radial engagement of the tool, the cutting mechanics change from shear mode to frictional rubbing mode, and therefore, cutting pressure coefficients begin to increase. As shown in Fig. 9 and considering the overprediction of K_t in test series CFC6, CFC7, and CFC9, by reducing the radial immersion in these tests, the tangential cutting pressure starts to increase and therefore, the difference error (overprediction) between K_t of this test series and K_t values of the trochoidal test series starts to get even bigger. However, the difference error (underprediction) in radial cutting pressure coefficient shown in Fig. 10 can be potentially reduced by lowering the radial immersion of the tool in the slot-milling test series. To test this hypothesis, test ITS-3 of Table 1 was selected. The maximum uncut chip thickness of each chip in the first replication of this test is shown in Fig. 11a. Using the peak of the curve, the maximum radial immersion of the tool (based on its radius of 8 mm) was calculated equal to 4%. Two milling tests were carried out which were similar to the test IS-3 of CFC6 series in Table 2, but instead of full radial immersion, the tests were conducted with 4% immersion (equivalent to radial engagement in trochoidal test ITS-3) and 15% immersion (an arbitrarily higher number to be used for comparison). The identified cutting pressure coefficients are compared in Fig. 11b. As expected, with decreasing radial engagement, the error in tangential cutting pressure K_t increased and the error in radial cutting pressure K_r decreased; therefore, the same conclusion described above can be reached.

6 Cutting force simulation in trochoidal milling

In Section 5, it was shown that the cutting pressure coefficients in trochoidal milling cannot be predicted with enough

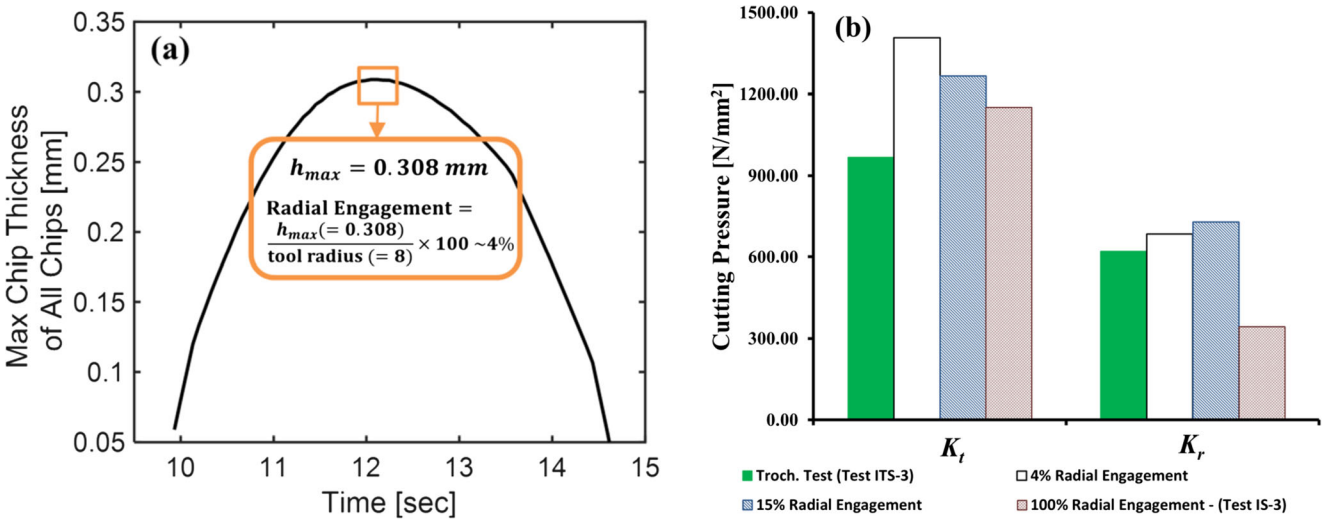

Fig. 11 Comparison of low radial engagement tests with trochoidal test ITS-3; **a** the maximum uncut chip thickness between all the chips is selected to define the trochoidal radial immersion and **b** cutting pressure comparison

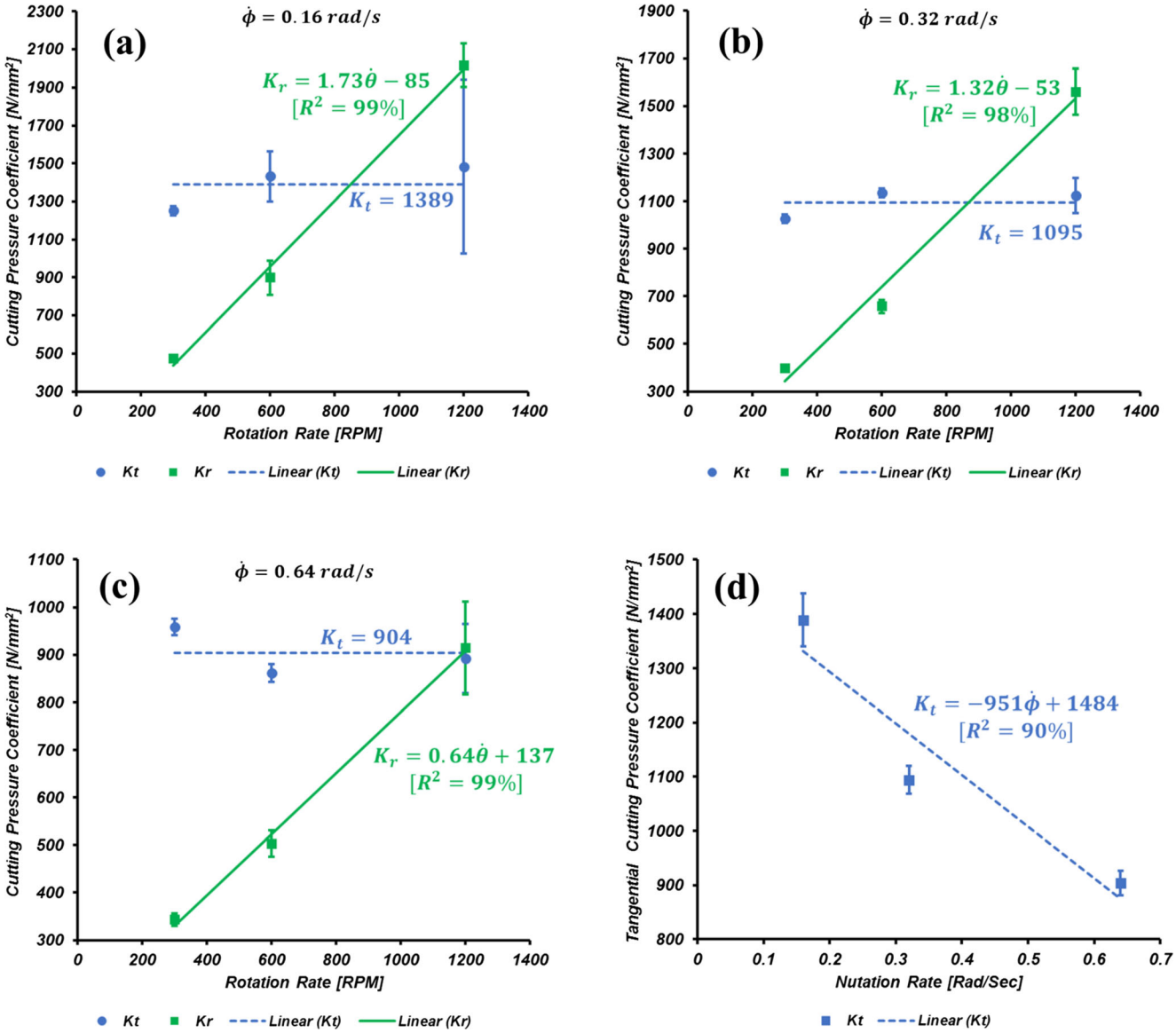

Fig. 12 Correlation of cutting pressure coefficients to rotation and nutation rates; **a** low nutation rate 0.16 rad/s, **b** medium nutation rate 0.32 rad/s, **c** high nutation rate 0.64 rad/s, and **d** tangential cutting pressure dependency on rotation rate

accuracy using conventional milling tests (slot milling with full or partial radial engagement). As a result, a separate set of experiments with trochoidal tool path is needed to establish the correlation of cutting pressure coefficients and tool path parameters. The DoE used in this section was already shown in Table 3 (tests series TS-1–9) and contains nine experiments (with three replications) in varying rotation and nutation rates as a training set with single-flute tool and four experiments

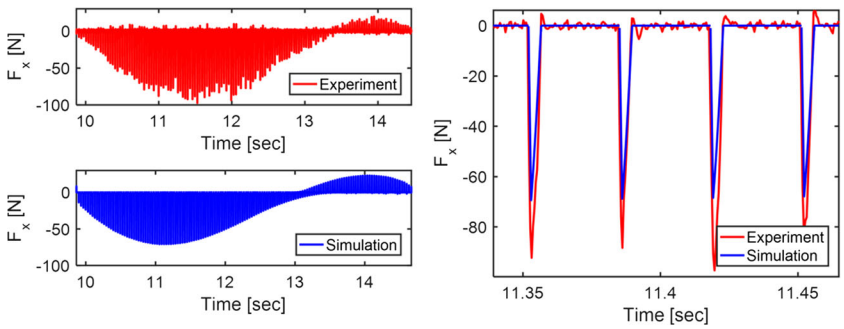

Fig. 13 Comparison of cutting forces in *X* direction between experiment and simulation for test TD-1

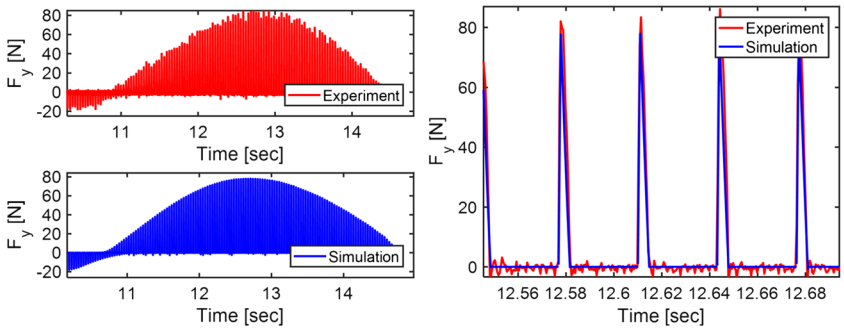

Fig. 14 Comparison of cutting forces in Y direction between experiment and simulation for test TD-1

with a two-flute tool as a testing set. The cutting pressure coefficients are identified for the training set and a linear regression model was fitted for each coefficient as shown in Fig. 12. From this, it is concluded that the tangential cutting pressure (K_t) is independent of rotation rate ($\dot{\theta}$) but demonstrates a linear dependency on nutation rate ($\dot{\phi}$) (see Fig. 12d). The radial cutting pressure (K_r) is linearly correlated to both rotation and nutation rates. The generalized linear regression models fitted to each coefficient are given in Eqs. (13) and (14). Using these equations, with known trochoidal tool path parameters, the cutting force coefficients, K_t and K_r, can be approximated and used in the semi-mechanistic force model of Eq. (11) to simulate cutting forces.

$$K_t = -951\dot{\phi} + 1484 \quad [R^2 = 90\%] \tag{13}$$

$$K_r = -1062\dot{\phi} + \dot{\theta} + 557 \quad [R^2 = 67\%] \tag{14}$$

6.1 Cutting force prediction in two-flute trochoidal milling

The testing set (tests TD-1–4) of Table 3 was used to (1) test the validity of the numerical uncut chip thickness calculation method described in Section 2 and (2) to investigate the accuracy of the proposed regression model of cutting pressure coefficients Eqs. (13) and (14) to simulate cutting forces in trochoidal milling. In the testing set, the nutation rate was kept constant ($\dot{\phi}$ = 0.64 rad/s) and the rotation rate was varied from 900 to 1450 RPM. First, the cutting pressure coefficients were calculated, and then Eqs. (11) and (12) were used to simulate the cutting forces in X and Y directions. The comparison between the simulated and experimental cutting forces of test TD-1 is shown in Figs. 13 and 14. Furthermore, this comparison for tests TD-2 to TD-4, where the force reaches its peak value, is given in Fig. 15, 16, and 17. To better quantify the simulation error, it was decided to compare the simulated forces in the X and Y directions to measured forces for ten chips in the region where force in X and Y directions reaches its peak value. The average error, standard deviation, and maximum error are shown in Fig. 18 and also given in Table 5. In general, the approach taken in this article shows better performance in predicting cutting force in Y (feed) direction with total average error of 8% between all four tests and maximum observed error of 45% (in test TD-4), while larger error was observed in predicting force in X (lateral) direction with total average error of 17% and maximum observed error of 36% (in test TD-4).

7 Summary, conclusion, and future direction

The objectives of the this work were the following: (1) to investigate the dependency of the cutting pressure coefficients on tool path and quantify the correlation of cutting parameters in trochoidal milling (i.e., rotation and nutation rates) to the tangential and radial cutting pressure coefficients and (2) to study the accuracy in predicting cutting forces of a geometrical uncut chip thickness model based on the numerical intersection-finding algorithm. The results show that the

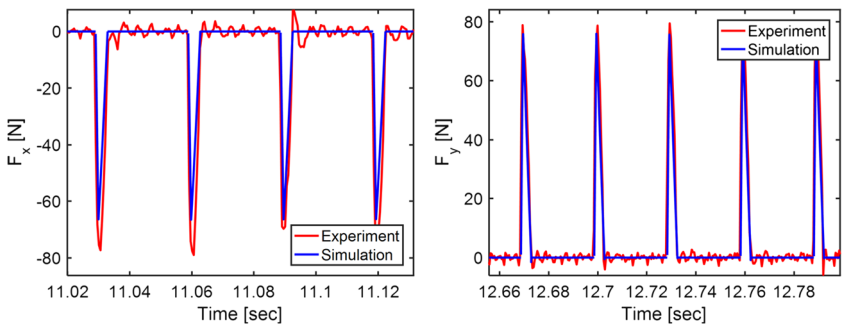

Fig. 15 Comparison of maximum cutting forces in X and Y direction between experiment and simulation for test TD-2

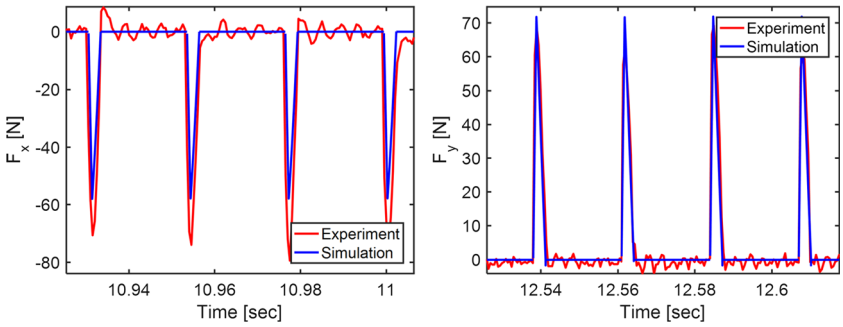

Fig. 16 Comparison of maximum cutting forces in *X* and *Y* direction between experiment and simulation for test TD-3

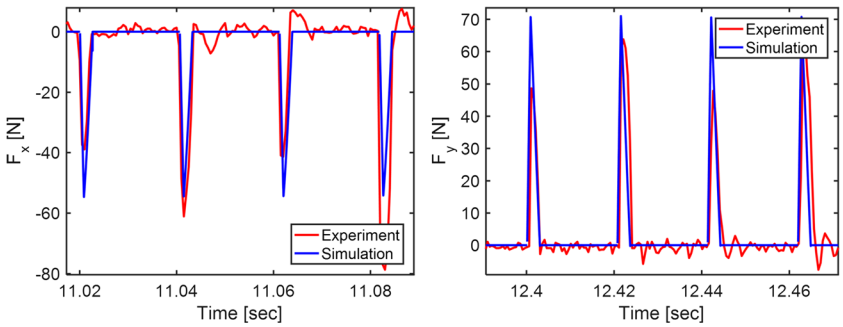

Fig. 17 Comparison of maximum cutting forces in *X* and *Y* direction between experiment and simulation for test TD-4

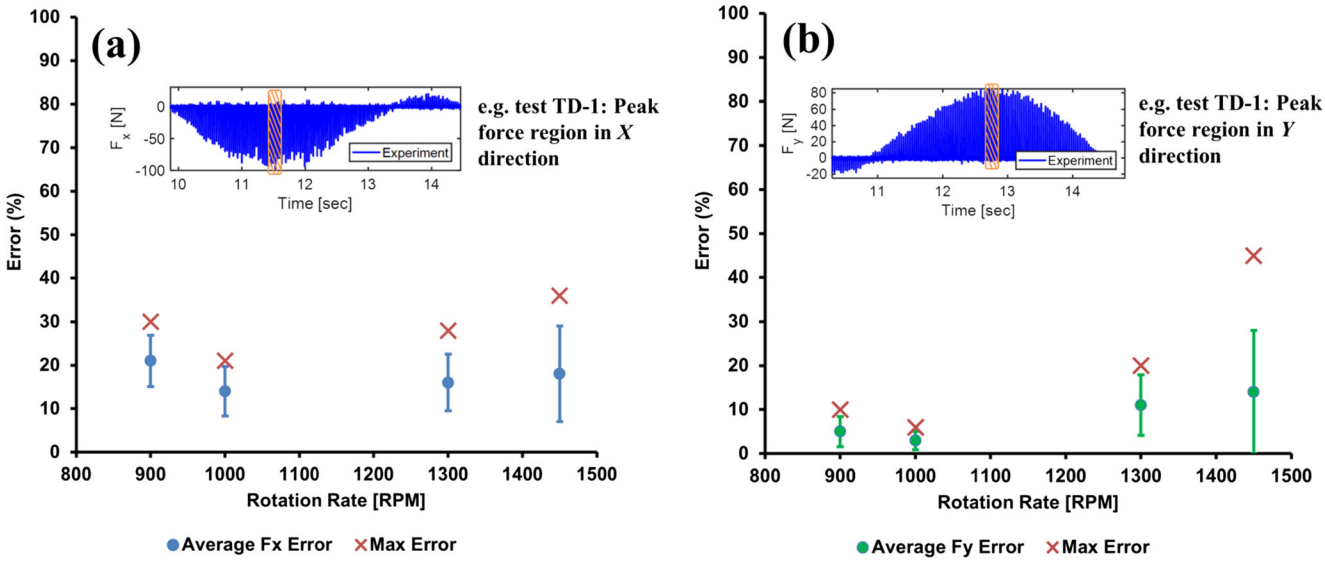

Fig. 18 Error comparison in **a** *X* direction and **b** *Y* direction. As an example, selected region of test TD-1 (containing ten chips) is shown as hatched orange where error values in *X* and *Y* directions are calculated

Table 5 Comparison of error and standard deviation between simulated and experimental cutting forces in *X* and *Y* directions in regions for ten chips with maximum force

Error in direction	Tests ID number (average error ± standard deviation)				Total average error (%)
	TD-1	TD-2	TD-3	TD-4	
X direction	21 ± 6	14 ± 6	16 ± 7	18 ± 11	17
Y direction	5 ± 3	3 ± 2	11 ± 7	14 ± 14	8

cutting pressure coefficients are significantly affected by the tool path parameters; it was concluded that unlike the previously published works on this subject where the cutting pressure coefficients were blindly taken from slot-milling tests, it is now apparent that these coefficients cannot be replaced as the cutting pressure coefficients of trochoidal milling. Hence, a separate design of experimental study with explicit trochoidal tool path is required. Furthermore, it was shown that the proposed uncut chip thickness algorithm is capable of predicting cutting forces in lateral and feed directions. To quantify the accuracy of the simulation, the maximum simulated force was compared with maximum measured force from the dynamometer for ten chips in the region where force in X and Y directions reached its peak. A total average error of 8% was observed in simulating cutting force in the feed direction and 17% total average error was observed in the lateral direction. Further steps taken in this article are summarized as below:

- The numerical algorithm was designed based on finding self- and cross-intersection points of the trochoidal tool path. A proper strategy was defined for connecting the intersection points and constructing the chip area. Furthermore, the numerical algorithm was generalized for uncut chip thickness modeling of multi-tooth and/or variable spacing cutting tools.
- A comprehensive DoE was designed to investigate the cutting pressure dependency on tool path and accuracy of force simulation. For cutting pressure extraction, 16 tests with 3 replications (a total of 48 tests) were carried out in slot milling using full radial engagement and trochoidal milling. Moreover, 9 tests with 3 replications (27 tests in total) were designed with a single-flute tool, and linear regression was used to develop a model of trochoidal tool path parameters and cutting pressure coefficients.
- A DoE with four new tests was designed with a two-flute tool in various rotation rates. The developed linear regression model was used to predict the cutting pressure coefficients which were integrated into the mechanistic force model for simulating the cutting forces. Finally, the simulated cutting forces were compared with experimental results and the corresponding error was reported.

In this article, the focus was solely given to the mechanics of cutting in trochoidal milling. However, dynamic stability of this alternative milling strategy is yet another important step for developing a comprehensive knowledge base on this topic. Unlike conventional milling operations, where the entering and exiting angle of the tool in the cut is consistent throughout the process, it is shown in this work that in trochoidal milling, these parameters vary as the tool marches in time and completes a full nutation. Therefore, the stability diagram in trochoidal milling evolves based on the location of the tool. This can potentially be advantageous as the critical depth of cut will change across the cut, possibly reducing the tendency to chatter. Investigation of this dynamic behavior of the cutting tool in a trochoidal tool path to identify chatter zone(s) and stability limits is the future direction of this work which will be addressed in a subsequent article.

Acknowledgments The authors would like to thank Mr. Douglas M. Schwarz of the University of Rochester for providing his source code for finding intersection points.

References

1. Djurdjanovic D, Mears L, Akhavan Niaki F, Ul Haq A, Li L (2017) State of the art review on process, system, and operations control in modern manufacturing. J Manuf Sci Eng. https://doi.org/10.1115/1.4038074
2. Toh CK (2003) Tool life and tool wear during high-speed rough milling using alternative cutter path strategies. Proc Inst Mech Eng Part B J Eng Manuf 217:1295–1304
3. Landers RG, Ulsoy AG (2000) Model-based machining force control. J Dyn Syst Meas Control 122:521–527
4. Denkena B, Flöter F (2012) Adaptive cutting force control on a milling machine with hybrid axis configuration. Procedia CIRP 4:109–114
5. Lee A-C, Lin M-T, Pan Y-R, Lin W-Y (2011) The feedrate scheduling of NURBS interpolator for CNC machine tools. Comput Des 43:612–628
6. Akhavan Niaki F, Michel M, Mears L (2016) State of health monitoring in machining: extended Kalman filter for tool wear assessment in turning of IN718 hard-to-machine alloy. SI NAMRC. J Manuf Process 24(Part 2):361–369
7. Pleta A, Ulutan D, Mears L (2014) Investigation of trochoidal milling in nickel-based superalloy inconel 738 and comparison with end milling. In: ASME 2014 International Manufacturing Science and Engineering Conference collocated with the JSME 2014 International Conference on Materials and Processing and the 42nd North American Manufacturing Research Conference. American Society of Mechanical Engineers, p V002T02A058-V002T02A058
8. Pleta A, Ulutan D, Mears L (2015) An investigation of alternative path planning strategies for machining of nickel-based superalloys. Procedia Manuf 1:556–566. https://doi.org/10.1016/J.PROMFG.2015.09.032
9. Uhlmann E, Fürstmann P, Rosenau B, et al (2013) The potential of reducing the energy consumption for machining TiAl6V4 by using innovative metal cutting processes. In: 11th Global Conference on Sustainable Manufacturing. Berlin, pp 593–598
10. Rauch M, Duc E, Hascoet J-Y (2009) Improving trochoidal tool paths generation and implementation using process constraints modelling. Int J Mach Tools Manuf 49:375–383. https://doi.org/10.1016/J.IJMACHTOOLS.2008.12.006
11. Shixiong W, Wei M, Bin L, Chengyong W (2016) Trochoidal machining for the high-speed milling of pockets. J Mater Process Technol 233:29–43. https://doi.org/10.1016/J.JMATPROTEC.2016.01.033
12. Szalóki I, Csuka S, Sipos S (2014) New test results in cycloid-forming trochoidal milling - Google Search. Acta Polytech Hung 11:1–14

13. Salehi M, Blum M, Fath B, Akyol T, Haas R, Ovtcharova J (2016) Epicycloidal versus trochoidal milling-comparison of cutting force, tool tip vibration, and machining cycle time. Procedia CIRP 46: 230–233. https://doi.org/10.1016/J.PROCIR.2016.04.001
14. Otkur M, Lazoglu I (2007) Trochoidal milling. Int J Mach Tools Manuf 47:1324–1332
15. Kardes N, Altintas Y (2007) Mechanics and dynamics of the circular milling process. J Manuf Sci Eng 129:21. https://doi.org/10.1115/1.2345391
16. Lawrence JD (1972) A catalog of special plane curves. Dover Publications, Mineola
17. Tlusty J (2000) Manufacturing processes and equipment. Prentice-Hall
18. Rubeo MA, Schmitz TL (2016) Milling force modeling: a comparison of two approaches. Procedia Manuf 5:90–105